

Optical Chirality Detection Using a Topological Insulator Transistor

Shouyuan Huang and Xianfan Xu*

Optical chirality is an effective means in screening molecules and their enantiomers in bioengineering, and recently has garnered attention as an implementation of qubits in quantum information processing. The conventional detection of circularly polarized light (CPL) is based on phase retardation and polarization separation using multiple optical components. An intrinsic solid-state chirality detection device would be favorable for easier integration and implementation. Optical spin injection to the spin-momentum-locked topological surface states of topological insulators (TIs) by circularly polarized light leads to a directional DC photocurrent and hence possible circular polarization detection. However, this DC photocurrent is also accompanied by other photo-responses. Here, a photodetection strategy using a TI transistor which senses CPL without the use of any additional components is demonstrated, it achieves a uniform response over the entire device with a sensitivity $\approx 5.6\%$. The Stokes parameters can also be extracted by arithmetic operation of photocurrents obtained with different bias and gate for a complete characterization of a polarized light beam. Therefore, this method enables chirality detection and Stokes parameter analysis using a single device. The proposed miniaturized intrinsic chirality detectors facilitate polarimetry sensing in applications from circular dichroism spectroscopy to biomedical diagnosis.

1. Introduction


Circular polarization of light describes the rotation of the direction of the electrical field vector as the light wave propagates. In nature, the handedness or chirality, clockwise or counter-clockwise of the E-field rotation, originates from light interactions with particular materials, especially organic molecules with chiral structures, and provides information in addition to the intensity and wavelength of light. In the vision systems of, for example, stomapods, circularly polarized light (CPL) is resolved to enhance contrast, recognize substances, and convey bioinformation.^[1] The optical absorptions in chiral molecules are different for left/right-handed CPL, thus the chirality detection

of CPL can serve as a molecule-screening tool. In fact, it is widely used in drug screening to discern effective medical target products from ineffective or even toxic enantiomers.^[2] The emerging applications in quantum communication and computing,^[3,4] circular dichroism spectroscopy, and polarimetric imaging^[5] also demand optical chirality detection. However, conventional solutions for optical chirality detection require multiple optical elements including phase retarders, quarter waveplate (QWP), polarizing beam splitters, and rotating optomechanical components. This is due to the lack of intrinsic chiral response in common semiconductors such as silicon and III–V semiconductors from which photodetectors are made, thus, miniaturization of optical chirality detection devices is challenging. One direction of seeking chirality detecting devices is using intrinsically chiral materials including chiral dyes and liquid crystals. The first organic-semiconductor transistor for chirality detection utilized chiral helicene^[6] and hybrid perovskite devices were explored by combining

the chiral-sensitive absorbing organic material and inorganic compound to enhance the optoelectronic performance.^[7,8] The invention of metamaterials or metasurfaces, that is, fabrication of sub-diffraction-limited nanostructures, enabled chiral optical properties beyond those offered by naturally existing materials. Metamaterials with helical nanostructures, for example, spirals that lack mirror symmetry, exhibit chirality-dependent absorption/transmission, and have been shown to achieve direct chirality detection.^[9–14] Alternatively, metamaterials and metasurfaces also demonstrated the capability of manipulating polarization states,^[15] and could function as ultracompact optical elements including linear/circular polarizers,^[11] waveplates/phase-retarders,^[16] and polarizing beam splitters.^[17] Fabricating these optical elements on top of conventional photodetectors can resolve the optical chirality^[18,19] or extract the full Stokes parameters.^[20]

Topological insulators (TIs) are a new phase of quantum materials with topological surface states (TSS) on the surface.^[21,22] Tetradymites are known as one of the best room-temperature thermoelectric materials for decades^[23–26] and also have been applied in optoelectronics,^[27–29] and later proven to be 3D TIs.^[30–33] The spin texture of the TSS electrons is locked to their momentum, so that the spin polarization can be induced

S. Huang, Prof. X. Xu
School of Mechanical Engineering and Birck Nanotechnology Center
Purdue University
West Lafayette, Indiana 47907, USA
E-mail: xxu@purdue.edu

 The ORCID identification number(s) for the author(s) of this article can be found under <https://doi.org/10.1002/adom.202002210>.

DOI: 10.1002/adom.202002210

by a current (electron motion with certain momenta),^[34–36] and conversely, spin injection to the TSS can lead to a measurable current.^[37] The quantum picture is that photons of CPL with the spin angular momentum of $\pm 1\hbar$ can interact with (flip) the electrons with spin $\mp \frac{1}{2}$ during a selective excitation according to angular momentum conservation. The optical injection of spin polarization of TSS results in a circularly-polarized-light-controlled photocurrent which is phenomenologically called circular photogalvanic effect (CPGE) and is naturally a candidate for chirality detection. However, CPGE is accompanied by additional photocurrents originated from other mechanisms.^[37–41] The combined optoelectronic effects can be seen when using a QWP at an angle α to convert a certain portion of linear polarized light to CPL, and the circular polarization has a $\sin 2\alpha$ dependence. The output with various QWP angles α can be viewed as simulating a light beam with different circular and linear components, expressed as:

$$J = D + C \sin 2\alpha + L_1 \sin 4\alpha + L_2 \cos 4\alpha \quad (1)$$

In Equation (1), the C term is the desired circular photoresponse for chirality detection. L_1 and L_2 are linear photoresponses and may be attributed to linear photogalvanic effect (LPGE) or photon drag effect due to lack of inversion symmetry at its surface states.^[42–44] Both C and L terms are highly dependent on the intrinsic chemical potential,^[39,45] which is sensitive to the surface condition.^[46–48] The polarization insensitive D term can originate from photothermoelectric (PTE) and photovoltaic effect,^[37,38,49,50] and are highly dependent on the location on the TI surface where the light interacts with it. These additional photoresponses make it

difficult to use spin-momentum locked TSS as reliable optical chirality detectors.

In this work, we report realization of intrinsic optical chirality detectors using thin-film topological insulator $\text{Bi}_2\text{Te}_2\text{Se}$ transistors. We found that photoconductance is sensitive to CPL when proper back-gating is applied and is independent of linear polarization regardless of the chemical potential. Moreover, the circular photoconductance is nearly uniform throughout the device. In addition, the $\text{Bi}_2\text{Te}_2\text{Se}$ phototransistor can be tuned into the linear polarization detection mode and the Stokes parameters can be extracted. The implementation of single-device, intrinsic optical chirality detection with minimum requirements for microfabrication will make it ready for multiple fields of applications.

2. Results and Discussion

The TI phototransistor is fabricated from exfoliated $\text{Bi}_2\text{Te}_2\text{Se}$ thin films. All the optical experiments are performed using a 633-nm He-Ne laser at room temperature. The schematics in Figure 1a shows the light beam with controlled polarization states obliquely incident on the phototransistor at certain source-drain bias voltage V_{ds} and back-gate voltage V_{gs} . The detailed fabrication procedure and experimental method/conditions can be found in Experimental Section.

We first show in Figure 1b the measured photocurrent versus QWP angle α of an 11-nm $\text{Bi}_2\text{Te}_2\text{Se}$ thin-film transistor under unbiased and ungated condition ($V_{gs} = 0$ V, $V_{ds} = 0$ V, the curve with red open circles). The photocurrent responds to both circular and linear polarized light as seen in the finite values of

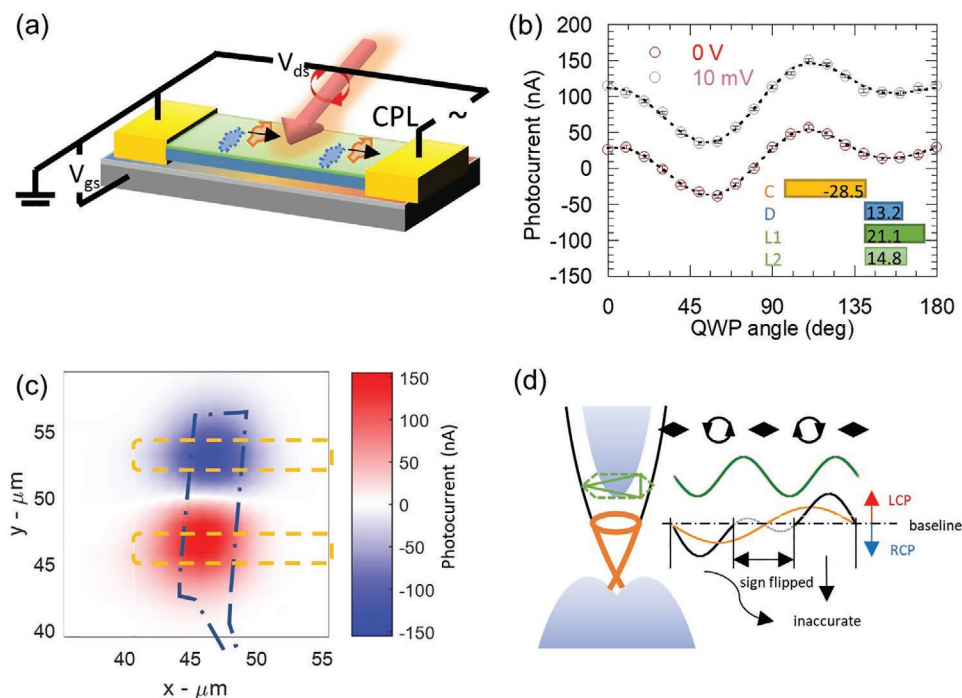


Figure 1. Photocurrent in $\text{Bi}_2\text{Te}_2\text{Se}$ thin film. a) Schematics of experimental setup; b) photocurrent under $V_{ds} = 0$ and 10 mV versus polarization (QWP angle) of an 11-nm thick $\text{Bi}_2\text{Te}_2\text{Se}$ device under $V_{gs} = 0$ V; c) photocurrent mapping of an 11-nm thick $\text{Bi}_2\text{Te}_2\text{Se}$ device; and d) schematics of the band structure of $\text{Bi}_2\text{Te}_2\text{Se}$ and the photocurrents resulting from a different mechanism.

the fitted C (circular response) and L_1 and L_2 (linear response) terms in the inset of Figure 1b, similar to the results reported in literature^[37–40] and our previous work.^[41] This result is obtained by focusing the light at the center of the device, which is determined from photocurrent mapping shown in Figure 1c. The geometry of the contacts for the device is marked by dashed lines. The photocurrent in Figure 1c is largely from the photo-thermoelectric effect. In principle, chirality detection can be realized by comparing the photocurrent with the anticipated circular polarization response to the polarization-insensitive baseline, for example, photocurrent less than the baseline indicating a net right circular polarization (RCP) component in the light beam and greater than the baseline indicating a net left circular polarization (LCP) component as illustrated in Figure 1d. Although the results of photocurrent versus QWP angle in Figure 1b show a clear optical chirality dependence, however, the distortion from an ideal $\sin 2\alpha$ trend due to the additional linear polarization response prevents it from accurate

quantification of the circular polarization component. As illustrated in Figure 1d, in the cases with larger L_1 , L_2 terms (here we sketched the case of $L_1 \sim C$), the photoresponses between $\approx 60^\circ < \alpha < \approx 120^\circ$ are mostly due to linear polarization, and the LCP/RCP can even be incorrectly determined (the dashed section of the black curve flips the polarity to the opposite side of the baseline).

The important finding of this work is that the photoresponse from circular polarization can be unambiguously separated from linear polarization by obtaining the differential photocurrent at different bias voltages, that is, by subtracting the photocurrent under 0 V from that under 10 mV bias voltage in Figure 1b. The differential photocurrent shown in Figure 2a can be well-fitted using only two terms, the circular photoresponse $C \sin 2\alpha$ and the polarization-insensitive D term. Hence, the differential photocurrent is sensitive solely to the circular polarization but not to the linear polarization. We attribute amplification/suppression of circular polarization-dependent photocurrent

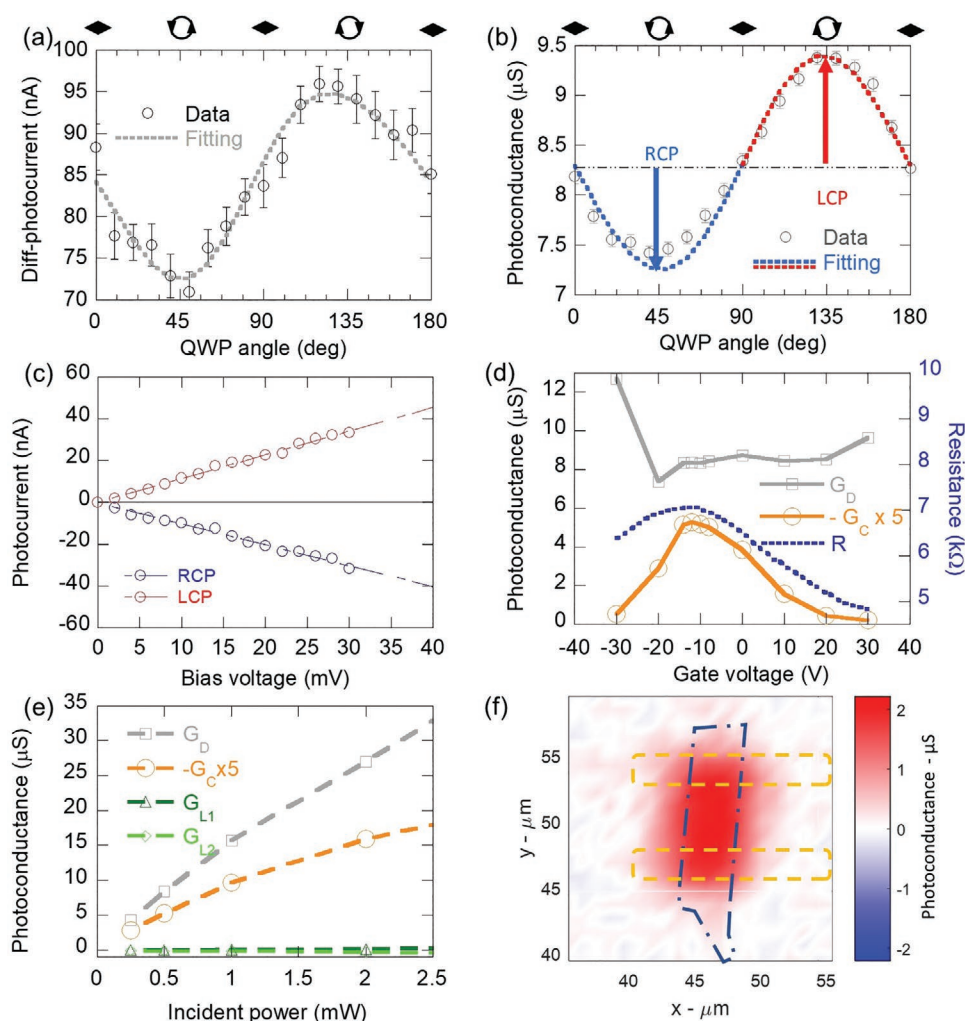


Figure 2. Polarization dependent photoconductance in an 11-nm thickness BTS device. a) Differential photocurrent versus polarization (QWP angle) of the 11-nm thick Bi₂Te₂Se device obtained with 0 and 10 mV bias. b) Photoconductance versus polarization (QWP angle), obtained by photo I - V sweep, with an incident laser power ≈ 0.5 mW, $V_{gs} = -12$ V; and c) scaled photocurrent versus bias voltage under RCP, LCP incidence. d) Photoconductance and device resistance versus gate voltage under an incident power ≈ 0.5 mW; e) photoconductance components (G_D , G_C , G_{L1} , and G_{L2}) versus incident power, measured at $V_{gs} = -12$ V; and f) mapping of the photoconductance contrast between LCP and RCP incidences.

under bias to the combined effect of the current-induced spin imbalance in the spin-polarized TSS channel and the optical selection of the spin-momentum locked TSS. The measurable helical differential photocurrent is enabled by the long spin-relaxation time of TSS electrons generated by circular polarized light. It has been found that optically injected spin polarization persists for over 10 ps, covering the entire energy relaxation process.^[51] The spin lifetime covers numerous momentum relaxations of electrons in the bias voltage drift current hence the spin-selectively generated TSS carriers persistently contribute to the conduction due to spin-momentum locking. The differential photocurrent under circularly polarized excitation can thus be understood as a spin-dependent photoconductance due to photogenerated carriers with persisting spin polarization, in addition to the helical current at zero bias. On the other hand, the linear polarization-dependent photocurrent is not amplified by the bias because of its instantaneous nature of the LPGE (Note S1, Supporting Information), which is not affected by a DC voltage/current. The ultrafast shift current or accumulation of electron momenta that leads to LPGE relaxes in a much shorter timescale (<100 fs)^[52–54] and thus only contributes to the photocurrent but not photoconduction. We found that the differential photocurrent solely depends on circular polarization for all the devices studied with thicknesses of the devices ranging from ≈10–70 nm (results of other devices are presented in Note S2, Supporting Information).

In Figure 2b, we show the photoconductance obtained at the bias of $V_{ds} = 10$ mV ($V_{gs} = -12$ V) against QWP angles, which can be fitted using $G = G_D + G_C \sin 2\alpha$. The maximum and minimum values obtained at RCP (at $\alpha = 45^\circ$) and LCP (at $\alpha = 135^\circ$) are marked by blue and red vertical arrows. To improve the accuracy of the photoconductance measurement, especially the circular photoconductance G_C that is related to circular polarization detection, the photocurrent is measured at different bias voltages in I–V sweeps. In Figure 2c, we show the photocurrent $I_{d,ph}$ from circular polarization (by subtracting the unpolarized component and the value at zero bias) versus V_{ds} , together with their linear fit for obtaining G_C (the dashed line). The $I_{d,ph}$ – V_{ds} curve shows a good linear fit for G_C . The averaged uncertainty of the photoconductance or the deviation from the fitting of the slope is ≈5.6%. Using this slope or the photoconductance as a measure for polarization can thus greatly improve the sensitivity compared with merely the differential photocurrent obtained at one V_{ds} in Figure 2a,b.

The back-gate voltage also affects photodetection. The optimized condition for circular polarization detection is obtained by maximizing G_C versus back-gate voltages, which is found to be ≈–12 V as shown in Figure 2d. Two-terminal resistances of the device R versus V_{gs} are also plotted in Figure 2d, illustrating the chemical potential in the 11-nm film is effectively tuned by the back-gate (the depletion layer thickness at this back gate voltage is ≈30 nm^[41]). The peak of the resistance corresponds to the approximate location of the charge-neutral point (CNP), where the optimized condition for circular polarization detection is also located. The reason is that the chemical potential near CNP provides a minimum Coulomb blockade during the spin-selective excitation. As the chemical potential moves towards the bulk bands, the increased rate of scattering out of TSS also contributes to the drop of the circular photoresponse.

In addition, the CNP is away from the trivial bands so PTE and LPGE effects are reduced. Therefore, the circular photoresponse is maximized near CNP. Photoconductance is further investigated with increased incident intensity. Figure 2e shows no sign of saturation till the maximum available power. The photoresponsivity of the (total) light intensity and CPL intensity are extracted to be 1.66 and 0.21 mA W^{–1}, respectively. We notice photoresponsivities of chirality detectors as high as 797^[7] and 280 mA W^{–1}^[8] can be achieved using chiral perovskite. In this work, we conservatively applied a 30 mV bias voltage to avoid degradation and ensure repeatability throughout all the tests (otherwise the intrinsic chemical potential may shift and the optimized gate voltages would vary), comparing with the 20 and 0.5 V used in literature. Hence when more effective passivation is available, a larger bias voltage can be applied and the photoresponsivity is expected to improve. On the other hand, the increased dark current, though demodulated using the lock-in technique, determines noise-equivalent power and results in an upper bound of the sensitivity (currently, the noise level under largest bias is ≈400 pA).

The results shown above are obtained at the center of the device where the thermoelectric effect is minimum. However, photoconductance of circular polarization G_C is nearly uniform with a variation less than 5% across the entire device as shown in Figure 2f. Here, the photoconductance G_{LCP} and G_{RCP} are acquired for both LCP and RCP incidences, obtained from the differential photocurrents under 0 and 30 mV bias voltage, and the differences of the two, $G_c = \left[G\left(\alpha = \frac{\pi}{4}\right) - G\left(\alpha = \frac{3\pi}{4}\right) \right] / 2$, are mapped over the entire device. The photocurrent generated from PTE that has a large spatial variation is only weakly dependent on the bias voltage and is therefore canceled. This is because the PTE photocurrent depends on the temperature rise caused by laser heating but little on the bias. This indicates that circular photoconductance of TI transistors can be used to measure CPL with random shapes of the light beam and does not require focusing of the light beam to a certain location.

Figure 2 provides the basis for characterizing the chirality of a light beam. To use a device for measurements, the polarization-insensitive photoconductance G_D and the chirality-sensitive photoconductance G_C can be obtained to produce a power-dependent calibration chart (Figure 2e), which can be converted to the photoconductance per unit irradiation power. G_D and G_C are then used to produce a photo-output characteristic graph similar to Figure 2c for a given incident power. When using the device for polarization measurement, $I_{d,ph}$ versus V_{ds} are measured which result in a line between the LCP (red) and RCP (blue) lines in Figure 2c. The irradiation is partially LCP (RCP) if the measured line has a positive (negative) slope. The $\sin 2\alpha$ behavior of circular polarization-dependent photoconductance (Figure 2b) indicates that the measured slope is proportional to the percentage of circular polarization. The degree of chirality, that is, the percentage of circular component $p_C = p_{CPL} / p_{total}$ of an elliptical polarized light beam can then be quantified using the ratio of the measured and calibrated slope. The aforementioned uncertainty of photoconductance (the slope of the curve) of 5.6% indicates that the chirality of a light beam with a circular polarization component larger than 5.6% can be discerned. Hence, this uncertainty can be defined as the

chiral sensitivity for characterizing the performance of chirality detection. For comparison, metamaterial-based chirality detectors and circular polarization filters are often characterized by the circular polarization extinction ratio (CPER, the ratio of the transmissivity of one chirality to the other), and the inverse of CPER, 1/CPER also indicates the percentage of circular polarization above which the chirality can be discerned. Therefore, we can compare our uncertainty with 1/CPER. The reported metamaterial-based detection has reached a CPER = 35, that is, chiral sensitivity $\approx 3\%$.^[20] However, our device, using intrinsic physical properties of TI, requires much less efforts in fabrication.

We also observed that circular photoconductance does not increase with the thickness of devices (Note S2, Supporting Information), further confirming the TSS origin, which is different from the (in-plane) bulk spin Hall effect mechanism of photoconductance on the edges as reported in Ref. [55]. The difference in the dominating mechanism is mainly due to the dimensions in the spin-selection direction versus the spin-Hall current direction. The spin potentiometry measurements on the top surface of Bi₂Te₂Se thin films^[34,36] also revealed the TSS contribution is much greater than that of bulk spin Hall effect. Because the origin of the circular photoconductance is the TSS with gapless Dirac dispersion, the chirality detection can also operate under lower energy excitation and even in mid-infrared (MIR) which can be used to directly measure the chiral thermal radiation from special texture or materials.^[1,56] An example of MIR chirality detection is presented in Note S3, Supporting Information.

Figure 2d shows the circular photoconductance varies greatly with back gate, from a peak value at $V_{gs} \approx -12$ V to near zero when $V_{gs} = 20$ V, due to the chemical potential moving from CNP to the conduction band edge. On the other hand, the polarization insensitive component of photoconductance (G_D) varies only slightly in a wide range of back-gate voltage from -20 V $< V_{gs} < 20$ V. As discussed previously, the chemical potential resides in the bulk bandgap in this range of back-gate voltage. The photoconductance depends on the generated carrier density, which is determined by the product of optical absorbance and relaxation time. When the chemical potential resides in the bulk bandgap, the absorbance (optical transition rate) is proportional to the TSS density of states (DOS), while the relaxation time in TSS is inversely proportional to the DOS,^[57] resulting in a constant photoconductance. The constant photoconductance from non-polarized light and varied photoconductance from polarized light provides a simplified approach in the measurement. When measuring a light beam with unknown intensity, we can first measure the (total) G at a large positive bias, for example, $V_{gs} = 20$ V, which reflects the total irradiation intensity. This G is then subtracted from the total G measured under $V_{gs} = -12$ V to obtain the circular component. This substitution of G_D (at $V_{gs} = -12$ V) with G at $V_{gs} = 20$ V enables measurement of chirality without the knowledge of the irradiation intensity, but at a cost of introducing a slightly larger uncertainty in obtaining G_C and a chiral sensitivity of $\approx 10\%$. We found this strategy is applicable for devices with a thickness below 15 nm. Thicker devices are more challenging because the back-gate does not effectively tune the chemical potential throughout the thickness of the device.^[41] Details are shown in Note S2, Supporting Information.

Lastly, we discuss using the same TI device for full polarimetry imaging so as to resolve the complete polarization states. The plane wave polarization state is characterized by a set of independent Stokes parameters, namely $S_0 = E_x E_x^* + E_y E_y^*$ representing the total intensity, $S_1 = E_x E_x^* - E_y E_y^*$ and $S_2 = E_x E_y^* + E_y E_x^*$ characterizing the linear polarization, and $S_3 = i(E_x E_y^* - E_y E_x^*)$ quantifying the degree of circular polarization.^[58] We already showed in the photoconductance measurement that the total intensity (I , Equation (2)) of the light beam, the intensity (or percentage) of the circular component (Equation (3)), and the chirality can be obtained. When the light is elliptically polarized (a combination of linear and circular polarized light with a degree of polarization $p = 1$, Equation (4)), the only remaining parameter is the orientation of linear polarization (ψ , Equation (5)), since the amplitude of the linear polarization can be obtained from the difference between the total and circular polarization components.

$$I = S_0 \quad (2)$$

$$p_c = S_3/S_0 \quad (3)$$

$$p = \sqrt{S_1^2 + S_2^2 + S_3^2}/S_0 = 1 \quad (4)$$

$$\tan(2\psi) = S_2/S_1 \quad (5)$$

The LPGE is used here to characterize the linearly polarized light. To obtain the optimized condition for linear polarization measurement, gate-dependent photocurrents are obtained and are shown in Figure 3a. At a large positive gating, $V_{gs} = 30$ V, the helicity-controlled photocurrent is completely turned off and thus it is an ideal condition for linear polarization detection. This is because the chemical potential is tuned to the warping region at the conduction band edge where the spin texture is not strictly locked to momentum.^[46] Also, the electrons are easily scattered to spin-degenerated states.^[41,46] The trivial states due to the band-bending on the surface are further filled with the increase of the back-gate voltage. The LPGE current also turns up with the gate voltage. Thus the observed enhancement of LPGE may be explained by the increased free carrier density (Note S1, Supporting Information). The photocurrent resulting from linear polarization incidence is plotted versus the angle of the QWP α or half the polarization angle ψ in Figure 3b and shows a clear linear polarization dependence that can be expressed as a function of $J = 35.5\cos(4\alpha + 0.16\pi) = 35.5\cos(2\psi + 0.16\pi)$ nA. An angle of 0.16π exists in the fitted function because photoresponse from linearly polarized light is related to the lattice orientation as discussed in Notes S1 and S2, Supporting Information, and the a -axis of the lattice is not intentionally aligned with the channel during fabrication. This angle can be easily calibrated with measurements shown in Figure 3b. The measured current is then used for determining the polarization angle ψ , which can be plugged into Equations (2)–(5) to find the Stokes parameters S_{0-3} .

3. Conclusion

This work demonstrated a single TI transistor device for optical chirality detection. By setting the phototransistor in different

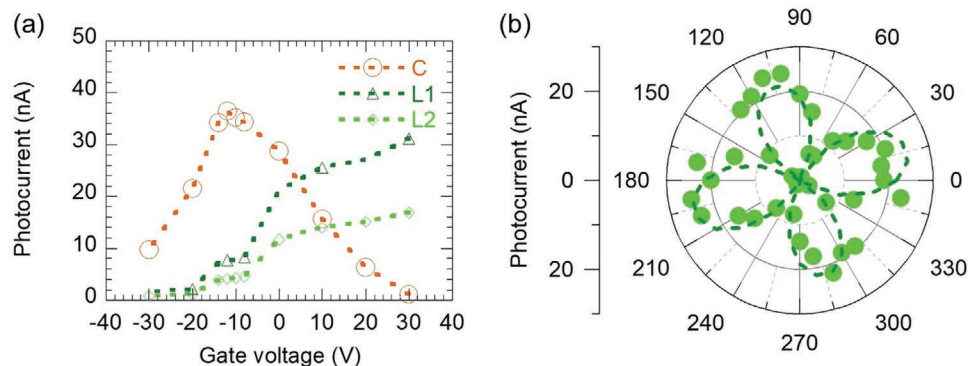


Figure 3. Linear polarization photocurrent response in an 11-nm thickness BTS device. a) Photocurrent components versus gate voltage under an incident power ≈ 0.5 mW; and b) photocurrent versus polarization (QWP angle) in the radial coordinate, measured at the device center, with an incident laser power ≈ 0.5 mW and back gate voltage $V_{gs} = 30$ V.

operating modes with combinations of bias and gate voltages, the circular and linear photoresponses can be switched on or off. The direct measurements of photocurrent that depends on circular polarization only and is spatially uniform will enable chiral photodetectors with a miniature device. The full Stokes parameters are extracted by incorporating the measured linear-polarization sensitive photocurrent on the same device. Therefore, the TI phototransistor shown in this work is an effective way for chirality and polarimetry detection, and can be used in a wide spectrum of applications from polarimetric imaging to biomedical molecules screening.

4. Experimental Section

Device Fabrication: The TI thin films were exfoliated using Nitto dicing tapes from $\text{Bi}_2\text{Te}_2\text{Se}$ bulk crystals grown by Bridgeman method, and then transferred onto a 50-nm SiO_2/Si substrate. A 0.7-nm Al layer was evaporated (then naturally oxidized into Al_2O_3 when exposed to air) to protect the sample surface. The contact was patterned by e-beam lithography, dipped in buffered oxide etcher to remove the Al_2O_3 , and deposited by evaporation Cr/Au of 5/50 nm.

Photocurrent Measurements: The 633-nm He-Ne laser beam was focused by an off-axis mirror (spot size ≈ 5 μm) and incident to the sample at 45° and modulated by a mechanical chopper at 822 Hz. The photocurrent was first amplified/filtered by a current-preamplifier then measured by a lock-in amplifier at the chopping frequency. The bias voltage was supplied by the current-preamplifier and the gate voltage (across the source contact and doped-Si gate) was supplied by a DC source-meter grounded at the same potential as the amplifiers. The mapping was realized by synchronizing the current measurement with a piezoelectric nano-positioner. All measurements were performed at room temperature.

Supporting Information

Supporting Information is available from the Wiley Online Library or from the author.

Acknowledgements

This work is partly supported by the National Science Foundation, EFMA-1641101 and CBET-1804377. The authors thank Y. P. Chen

and I. Miotkowski for providing the material. They also thank A. E. Llacahuanga Allcca, J. Tian, V. Iyer, and Y. Xu for valuable discussions on experimental designs and device fabrication.

Conflict of Interest

The authors declare no conflict of interest.

Data Availability Statement

The data that support the findings of this study are available from the corresponding author upon reasonable request.

Keywords

chiral photodetectors, circular polarization, polarimetry imaging, Stokes parameters, topological surface states

Received: December 20, 2020

Revised: February 18, 2021

Published online:

- [1] T. H. Chiou, S. Kleinlogel, T. Cronin, R. Caldwell, B. Loeffler, A. Siddiqi, A. Goldizen, J. Marshall, *Curr. Biol.* **2008**, *18*, 429.
- [2] W. H. Brooks, W. C. Guida, K. G. Daniel, *Curr. Top. Med. Chem.* **2011**, *11*, 760.
- [3] C. Wagenknecht, C. M. Li, A. Reingruber, X. H. Bao, A. Goebel, Y. A. Chen, Q. Zhang, K. Chen, J. W. Pan, *Nat. Photonics* **2010**, *4*, 549.
- [4] J. F. Sherson, H. Krauter, R. K. Olsson, B. Julsgaard, K. Hammerer, I. Cirac, E. S. Polzik, *Nature* **2006**, *443*, 557.
- [5] G. C. Giakos, *IEEE Trans. Instrum. Meas.* **2006**, *55*, 1628.
- [6] Y. Yang, R. C. Da Costa, M. J. Fuchter, A. J. Campbell, *Nat. Photonics* **2013**, *7*, 634.
- [7] C. Chen, L. Gao, W. Gao, C. Ge, X. Du, Z. Li, Y. Yang, G. Niu, J. Tang, *Nat. Commun.* **2019**, *10*, 1927.
- [8] A. Ishii, T. Miyasaka, *Sci. Adv.* **2020**, *6*, eabd3274.
- [9] A. Y. Zhu, W. T. Chen, A. Zaidi, Y. W. Huang, M. Khorasaninejad, V. Sanjeev, C. W. Qiu, F. Capasso, *Light: Sci. Appl.* **2018**, *7*, 17158.
- [10] W. Li, Z. J. Coppens, L. V. Besteiro, W. Wang, A. O. Govorov, J. Valentine, *Nat. Commun.* **2015**, *6*, 8379.
- [11] J. K. Gansel, M. Thiel, M. S. Rill, M. Decker, K. Bade, V. Saile, G. von Freymann, S. Linden, M. Wegener, *Science* **2009**, *325*, 1513.

- [12] W. Chen, D. C. Abeyasinghe, R. L. Nelson, Q. Zhan, *Nano Lett.* **2010**, *10*, 2075.
- [13] B. Frank, X. Yin, M. Schäferling, J. Zhao, S. M. Hein, P. V. Braun, H. Giessen, *ACS Nano* **2013**, *7*, 6321.
- [14] M. Zhang, V. Pacheco-Peña, Y. Yu, W. Chen, N. J. Greybush, A. Stein, N. Engheta, C. B. Murray, C. R. Kagan, *Nano Lett.* **2018**, *18*, 7389.
- [15] A. Papakostas, A. Potts, D. M. Bagnall, S. L. Prosvirnin, H. J. Coles, N. I. Zheludev, *Phys. Rev. Lett.* **2003**, *90*, 4.
- [16] N. Yu, F. Aieta, P. Genevet, M. A. Kats, Z. Gaburro, F. Capasso, *Nano Lett.* **2012**, *12*, 6328.
- [17] M. D. Turner, M. Saba, Q. Zhang, B. P. Cumming, G. E. Schröder-Turk, M. Gu, *Nat. Photonics* **2013**, *7*, 801.
- [18] Y. Zhao, M. A. Belkin, A. Alù, *Nat. Commun.* **2012**, *3*, 870.
- [19] Y. Zhao, A. N. Askarpour, L. Sun, J. Shi, X. Li, A. Alù, *Nat. Commun.* **2017**, *8*, 14180.
- [20] A. Basiri, X. Chen, J. Bai, P. Amrollahi, J. Carpenter, Z. Holman, C. Wang, Y. Yao, *Light: Sci. Appl.* **2019**, *8*, 2047.
- [21] M. Z. Hasan, C. L. Kane, *Rev. Mod. Phys.* **2010**, *82*, 3045.
- [22] J. E. Moore, *Nature* **2010**, *464*, 194.
- [23] H. J. Goldsmid, R. W. Douglas, *Br. J. Appl. Phys.* **1954**, *5*, 386.
- [24] R. Venkatasubramanian, E. Siivola, T. Colpitts, B. O'Quinn, *Nature* **2001**, *413*, 597.
- [25] S. I. S. W. Kim, K. H. Lee, H. A. Mun, H. S. Kim, S. W. Hwang, J. W. Roh, D. J. Yang, W. H. Shin, X. S. Li, Y. H. Lee, G. J. Snyder, S. I. S. W. Kim, *Science* **2015**, *348*, 109.
- [26] J. P. Heremans, R. J. Cava, N. Samarth, *Nat. Rev. Mater.* **2017**, *2*, 17049.
- [27] Y. Zhou, L. Wang, S. Chen, S. Qin, X. Liu, J. Chen, D. J. Xue, M. Luo, Y. Cao, Y. Cheng, E. H. Sargent, J. Tang, *Nat. Photonics* **2015**, *9*, 409.
- [28] L. Wang, D. B. Li, K. Li, C. Chen, H. X. Deng, L. Gao, Y. Zhao, F. Jiang, L. Li, F. Huang, Y. He, H. Song, G. Niu, J. Tang, *Nat. Energy* **2017**, *2*, 17046.
- [29] L. Guo, B. Zhang, Y. Qin, D. Li, L. Li, X. Qian, F. Yan, *Sol. RRL* **2018**, *2*, 1800128.
- [30] H. Zhang, C. X. Liu, X. L. Qi, X. Dai, Z. Fang, S. C. Zhang, *Nat. Phys.* **2009**, *5*, 438.
- [31] Y. L. Chen, J. G. Analytis, J. H. Chu, Z. K. Liu, S. K. Mo, X. L. Qi, H. J. Zhang, P. H. Lu, X. Dai, Z. Fang, S. C. Zhang, I. R. Fisher, Z. Hussain, Z. X. Shen, *Science* **2009**, *325*, 178.
- [32] L. Fu, C. L. Kane, E. J. Mele, *Phys. Rev. Lett.* **2007**, *98*, 106803.
- [33] X. L. Qi, S. C. Zhang, *Rev. Mod. Phys.* **2011**, *83*, 1057.
- [34] J. Tian, S. Hong, I. Miotkowski, S. Datta, Y. P. Chen, *Sci. Adv.* **2017**, *3*, e1602531.
- [35] J. Tian, I. Miotkowski, S. Hong, Y. P. Chen, *Sci. Rep.* **2015**, *5*, 14293.
- [36] J. Tian, S. Hong, S. Sayed, J. S. Lee, S. Datta, N. Samarth, Y. P. Chen, *Nat. Commun.* **2019**, *10*, 1461.
- [37] J. W. Mclver, D. Hsieh, H. Steinberg, P. Jarillo-Herrero, N. Gedik, *Nat. Nanotechnol.* **2011**, *7*, 96.
- [38] C. Kastl, C. Karetzky, H. Karl, A. W. Holleitner, *Nat. Commun.* **2015**, *6*, 6617.
- [39] Y. Pan, Q. Z. Wang, A. L. Yeats, T. Pillsbury, T. C. Flanagan, A. Richardella, H. Zhang, D. D. Awschalom, C. X. Liu, N. Samarth, *Nat. Commun.* **2017**, *8*, 1037.
- [40] J. Duan, N. Tang, X. He, Y. Yan, S. Zhang, X. Qin, X. Wang, X. Yang, F. Xu, Y. Chen, W. Ge, B. Shen, *Sci. Rep.* **2014**, *4*, 4889.
- [41] S. Huang, I. Miotkowski, Y. P. Chen, X. Xu, *Sci. Rep.* **2020**, *10*, 16761.
- [42] H. Plank, L. E. Golub, S. Bauer, V. V. Bel'kov, T. Herrmann, P. Olbrich, M. Eschbach, L. Plucinski, C. M. Schneider, J. Kampmeier, M. Lanius, G. Mussler, D. Grützmacher, S. D. Ganichev, *Phys. Rev. B* **2016**, *93*, 125434.
- [43] P. Olbrich, L. E. Golub, T. Herrmann, S. N. Danilov, H. Plank, V. V. Bel'kov, G. Mussler, C. Weyrich, C. M. Schneider, J. Kampmeier, D. Grützmacher, L. Plucinski, M. Eschbach, S. D. Ganichev, *Phys. Rev. Lett.* **2014**, *113*, 096601.
- [44] H. Plank, S. N. Danilov, V. V. Bel'kov, V. A. Shalygin, J. Kampmeier, M. Lanius, G. Mussler, D. Grützmacher, S. D. Ganichev, *J. Appl. Phys.* **2016**, *120*, 165301.
- [45] K. N. Okada, N. Ogawa, R. Yoshimi, A. Tsukazaki, K. S. Takahashi, M. Kawasaki, Y. Tokura, *Phys. Rev. B* **2016**, *93*, 081403.
- [46] M. S. Bahramy, P. D. C. King, A. de la Torre, J. Chang, M. Shi, L. Patthey, G. Balakrishnan, P. Hofmann, R. Arita, N. Nagaosa, F. Baumberger, *Nat. Commun.* **2012**, *3*, 1159.
- [47] D. Kong, J. J. Cha, K. Lai, H. Peng, J. G. Analytis, S. Meister, Y. Chen, H. J. Zhang, I. R. Fisher, Z. X. Shen, Y. Cui, *ACS Nano* **2011**, *5*, 4698.
- [48] A. J. Green, S. Dey, Y. Q. An, B. O'Brien, S. O'Mullane, B. Thiel, A. C. Diebold, *J. Vac. Sci. Technol., A* **2016**, *34*, 061403.
- [49] Y. Yan, Z.-M. Liao, X. Ke, G. Van Tendeloo, Q. Wang, D. Sun, W. Yao, S. Zhou, L. Zhang, H.-C. Wu, D.-P. Yu, *Nano Lett.* **2014**, *14*, 4389.
- [50] J. Besbas, K. Banerjee, J. Son, Y. Wang, Y. Wu, M. Brahlek, N. Koirala, J. Moon, S. Oh, H. Yang, *Adv. Opt. Mater.* **2016**, *4*, 1642.
- [51] V. Iyer, Y. P. Chen, X. Xu, *Phys. Rev. Lett.* **2018**, *121*, 026807.
- [52] M. T. Pettes, J. Maassen, I. Jo, M. S. Lundstrom, L. Shi, *Nano Lett.* **2013**, *13*, 5316.
- [53] L. Braun, G. Mussler, A. Hruban, M. Konczykowski, T. Schumann, M. Wolf, M. Münzenberg, L. Perfetti, T. Kampfrath, *Nat. Commun.* **2016**, *7*, 13259.
- [54] X. Wang, L. Cheng, D. Zhu, Y. Wu, M. Chen, Y. Wang, D. Zhao, C. B. Boothroyd, Y. M. Lam, J. Zhu, M. Battiato, J. C. W. Song, H. Yang, E. E. M. Chia, *Adv. Mater.* **2018**, *30*, 1802356.
- [55] P. Seifert, K. Vaklinova, S. Ganichev, K. Kern, M. Burghard, A. W. Holleitner, *Nat. Commun.* **2018**, *9*, 331.
- [56] E. Khan, E. E. Narimanov, *Phys. Rev. B* **2019**, *100*, 081408.
- [57] R. F. Pierret, in *Advanced Semiconductor Fundamentals*, 2nd ed., Prentice Hall, Upper Saddle River, NJ **2003**.
- [58] W. H. McMaster, *Am. J. Phys.* **1954**, *22*, 351.